Electrochemically Controlled Nanopore and Crystal Structure Evolution in Zinc Oxide Nanorods

Weon Ho Shin, Tae Hoon Hwang, Yun Suk Huh and Jang Wook Choi

J. Electrochem. Soc. 2012, Volume 159, Issue 12, Pages A2143-A2147.
doi: 10.1149/2.020301jes

Journal of The Electrochemical Society, **159** (12) A2143-A2147 (2012)
0013-4651/2012/159(12)/A2143/5/$28.00 © The Electrochemical Society

Electrochemically Controlled Nanopore and Crystal Structure Evolution in Zinc Oxide Nanorods

Weon Ho Shin,[a] Tae Hoon Hwang,[a] Yun Suk Huh,[b,z] and Jang Wook Choi[a,c,*,z]

[a]*Graduate School of EEWS(WCU), Korea Advanced Institute of Science and Technology, Yuseong-gu, Daejeon 305-701, Korea*
[b]*Division of Materials Science, Korea Basic Science Institute, Daejeon, 305-333, Korea*
[c]*KAIST Institute Nano Century, Korea Advanced Institute of Science and Technology, Yuseong Gu, Daejon 305-701, Korea*

We investigate high aspect ratio ZnO nanorods during Li-battery cycling by stepwise characterization of their crystal structures and porosities. During the cycling, nonporous ZnO nanorods become porous and, as a result, the surface area of ZnO nanorods increases significantly. As the Li amount inserted and extracted increases, it was observed that nanopores progress from the surfaces to the cores of ZnO nanorods. Also, in the crystal structure viewpoint, the original single-crystalline structure of the pristine ZnO nanorods gradually turns into the polycrystalline during the pore progression. This investigation not only delivers detailed information on the morphology and crystal structures of one-dimensional ZnO nanostructures during the course of Li-battery operations, but also suggests that battery processes can be a useful means to manipulate the crystal structure and porosity of ZnO nanostructures.
 [DOI: 10.1149/2.020301jes]

Manuscript submitted January 30, 2012; revised manuscript received October 8, 2012. Published October 23, 2012.

Due to the superior energy and power densities, so far lithium ion batteries (LIBs) have been successfully used for a variety of mobile electronics. Currently, LIBs are expanding their territory into larger-scale applications including hybrid electrical vehicles (EVs) and utility power grids.[1] While the large-scale applications require substantial improvement in all of the cell aspects, such as energy density, rate capability, lifetime, and safety, the energy density has become more critical. For example, it is related directly to the driving distance per charge in the case of EVs.[2] As an effort to increase the energy densities of the cells, high capacity anode materials beyond the commercial graphite anodes have been developed. Alloy-based materials represented by silicon,[3–13] germanium,[14–16] and tin[17–19] as well as conversion reaction-based metal oxides[20–22] are good examples along this direction.

Among various metal oxides for conversion reaction-based anodes, nanostructured zinc oxide (ZnO) electrodes have also turned out to be promising as their specific capacities[23–26] (700 ∼ 1300 mAh g^{-1}) are usually 3 ∼ 4 times higher than those of established graphite (∼300 mAh g^{-1}). Beyond the specific capacity that is determined by the electrode material, other important properties in the battery performance such as cycle life and charging-discharging rates can be improved further when electrodes are formed in one-dimensional (1D) nanostructures. In particular, in the current study, we paid our attention mainly to 1D nanorods (NRs) with high aspect ratios. In previous research, a 1D core-shell structure of iron oxide (Fe_3O_4) electrodes exhibited a robust cycle life and good capacity retention at high power operations (up to 8C: charge-discharge ∼7.5 min).[27] In most cases, 1D nanostructures are suitable for robust cycle lives and fast charge-discharge rates because the structures allow for facile strain relaxation during cycling and efficient electronic/ionic transport. Also, compared to the case of particle, 1D nanostructured electrodes are more compatible with in situ transmission electron microscope (TEM) technique and contribute to deep understanding on the electrochemical processes of various emerging battery materials including silicon[28] and tin oxide.[29] In addition to the structural benefits, in the case of ZnO, the well-established synthetic procedures in both solution[30–32] and gas[33] phases for various 1D nanostructures are an additional advantage.

On the other hand, recently, it was reported[34] that battery processes can generate nanopores in some metal oxide particles, and these porous particles with large surface areas were applied for electrochemical catalysts and supercapacitor electrodes. However, their study was limited to the applications of the porous metal oxides but did not provide a detailed picture of how nanopores and crystal structures evolve in those electrochemical processes. Herein, in an effort to understand 1D ZnO nanostructures that accompany morphological and crystal structural changes during the course of battery processes, their porosity and crystal structures were investigated at various stages of electrochemical cycling in a stepwise manner.

Experimental

Preparation of single-crystalline ZnO NRs.— ZnO NRs were grown on stainless steel foil (McMaster-Carr, foil 304) that was cleaned thoroughly via sonication in acetone/methanol and a gentle oxygen plasma etching (50 W, 20 seconds). The substrates were spin-coated with a seed solution at 1000 rpm for 1 min. The seed solution was prepared by stirring a solution of zinc acetate in methanol (10 mM) for 2 hrs at 60°C. After spin-coating three times, NRs were grown in an aqueous solution consisting of zinc nitrate (25 mM), hexamethylenetetramine (25 mM) and polyethyleneimine (6 mM) at 90°C for 2 hrs.[35] The substrates were taken out of the aqueous solution and rinsed with deionized water.

Li-battery cycles for pore formation.— The procedures for cell preparation were the same as reported previously.[3] Briefly, Li-battery cycles were carried out by preparing pouch-type half cells with Li foil (Alfa Aesar) as counter/reference electrodes. The cells were assembled in an argon-filled glove box (oxygen and water contents below 1 and 0.1 ppm, respectively). 1 M $LiPF_6$ dissolved in ethylene carbonate/diethyl carbonate (EC/DEC, 1:1 v/v, Ferro Corporation) was used as electrolyte, and polyethylene membranes (Asahi Kasei) was used as separators. The electrochemical processes were done by galvanostatic scans at a 0.1 C rate. The pore progression from the surfaces to the cores of ZnO nanorods was monitored by preparing multiple samples that underwent different degrees of lithiation. The degree of lithiation was controlled by lithiation time.

Porosity measurements.— The battery-cycled ZnO NRs were soaked in acetonitrile overnight then washed further with ethanol and methanol to remove residues from the electrolyte. ZnO NRs were treated further to remove residual Li_2O by dipping the substrates in water for ∼48 hrs. XPS data showing the absence of Li even at depths of ∼30 nm inside the NRs confirm that our cleaning processes are robust. The cleaned NRs were removed from the substrates by sonication in methanol. Dried ZnO NRs weighing 50 ∼ 100 mg were used to obtain isotherms using a Micromeritics porosity analyzer (ASAP 2020). Before actual adsorption measurements, the samples were degassed at 250°C under vacuum for ∼10 hrs.

Characterization.— Scanning electron microscopy (SEM) and transmission electron microscopy (TEM) were performed to observe

*Electrochemical Society Active Member.
[z]E-mail: yshuh@kbsi.re.kr; jangwookchoi@kaist.ac.kr

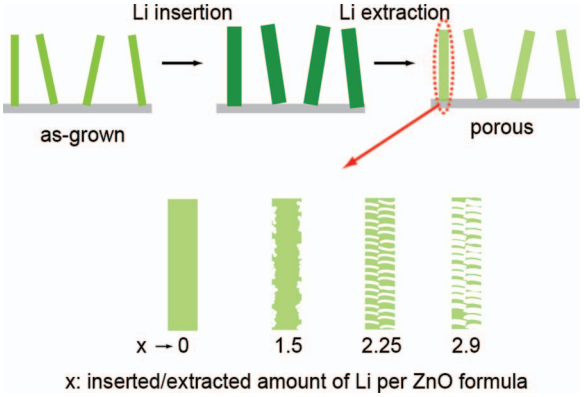

Figure 1. A schematic illustration of pore evolution in ZnO NRs. As the amount (=x value) of inserted and extracted Li per ZnO increases, pores penetrate from the surfaces to the cores of NRs, which is followed by the increase in the pore width.

the morphologies and crystallinity of ZnO NRs at various stages of battery cycling. X-ray photoelectron spectroscopy (XPS, ESCALAB250) with a Mg Ka line as an X-ray source was also conducted to ensure that the aforementioned washing process is effective in removing the residual Li_2O. The same washing processes as in the porosity measurements were conducted before the SEM, TEM, and XPS characterization.

Results and Discussion

As displayed in Fig. 1, as the Li amount inserted and extracted (x value) increases, it is expected that nanopores progress from the surfaces to the cores of ZnO NRs. In order to confirm this scenario, we first grew ZnO NRs directly onto stainless steel substrates as described in the Experimental section. As-grown NRs exhibit diameters of 40 $\sim$ 80 nm and lengths of 1 $\sim$ 2 μm (Fig. 2). TEM shows that as-grown NRs are single-crystalline with a <002> growth direction, as will be discussed at the end of this section.

The charging (lithiation) process of ZnO electrodes proceeds by a two-step process: a conversion reaction followed by an alloying reaction:

$$2Li + ZnO \leftrightarrow Li_2O + Zn \quad [1]$$

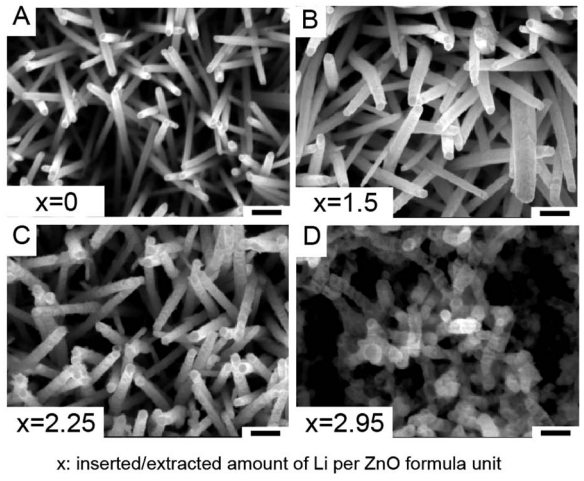

Figure 2. The morphology change of ZnO NRs as the amount (= x value) of inserted and extracted Li per ZnO increases. SEM images of NRs with (A) x = 0, (B) x = 1.5, (C) x = 2.25, and (D) x = 2.95 show rougher sidewalls with increasing x values. Scale bars are 200 nm.

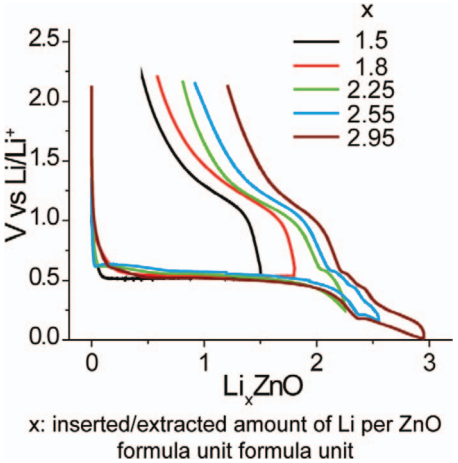

Figure 3. Electrochemical potential profiles in the charging and discharging processes for different x values (x = the amount of inserted and extracted Li per each ZnO). The C-rate was 0.1 C.

$$Zn + Li \leftrightarrow LiZn \quad [2]$$

Once zinc oxide is lithiated in the reaction 1, zinc nanograins are formed in a lithium oxide matrix.[20] If the lithiation proceeds further, the zinc nanograins become lithiated (reaction 2). Plateau locations around ~0.5 V as well as the relatively lower reversibility (Fig. 3) confirm the conversion reaction, and are also consistent with previous reports.[26,36] TEM characterization (Fig. 4A-4C) at the end of 1.5 Li insertion additionally supports the suggested conversion reaction mechanism: In the selected area electron diffraction (SAED) pattern (Fig. 4B), while a majority of spots are indexed to the lattice orientations of the unreacted ZnO, the polycrystalline rings indicative of Zn verify the Zn formation as a conversion reaction product. In the HRTEM image (Fig. 4C), lattice spacings of 0.28 and 0.205 nm, indicative of ZnO (100) and Zn (101) planes, were observed.

As the amount of Li inserted and extracted increases, we observed a morphology change away from the original straight sidewall. As shown in the SEM images in Fig. 2, the morphologies of NRs become rougher as the amount of Li inserted and extracted increases. More detailed information of the pore evolution was obtained by nitrogen (N_2) adsorption/desorption porosity measurements (Fig. 5). The N_2 adsorption/desorption isotherms (Fig. 5A) suggest some key features in the porosity of the NRs, such as stepwise pore evolution from partially porous to completely porous NRs as well as pore size increase after a certain point. As shown in Fig. 5B, the pore volume obtained by the BJH (Barret-Joyner-Halenda) method increases continuously with the amount of lithium inserted and extracted. By contrast, the BET (Brunauer-Emmett-Teller) surface area increases up to the point of 2.25 Li per ZnO but decreases thereafter. This trend of BET surface area suggests pore evolution from the surfaces to the cores of the ZnO NRs (Fig. 5B). Initially, pores are formed on the surface and the porous layer becomes thicker as more Li is inserted and extracted up to the point of 2.25 Li per ZnO. At this point, the pore evolution reaches the core of the NR and the entire NR becomes porous. This is also approximately consistent with a one-to-two stoichiometric ratio between ZnO and Li in the conversion reaction 1. Once the pore evolution passes this point, the pore widths become larger, causing the BET surface area to decrease. The pore size distribution (PSD) data (Fig. 5C) also paint a consistent picture: at the point of 1.5 Li per ZnO, the porous layer on the NR surface is so thin that the pores are exposed to the space outside the NRs and thus the pore widths turn out to be larger with a broader distribution. As more Li is inserted and extracted, the peak around 3.5 nm in the PSD gets sharper up to the point of 2.25 Li per ZnO, indicating pores with a narrower range of widths which persist throughout the entire NR. Beyond the point of

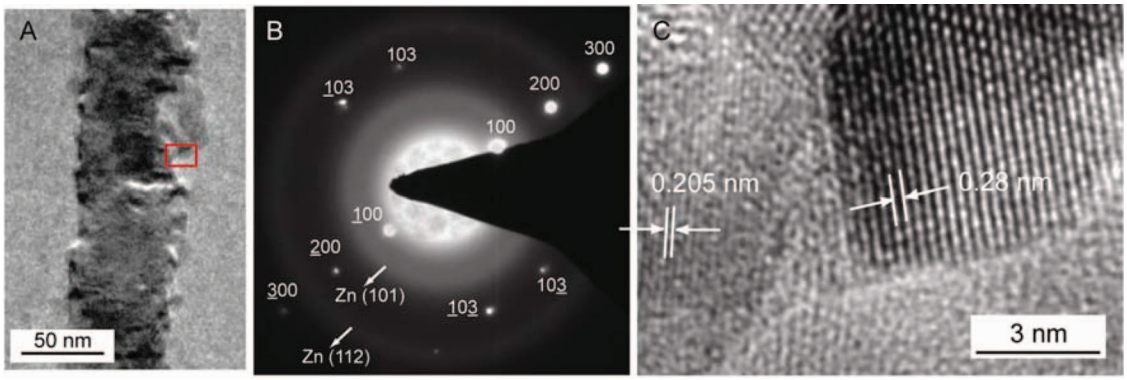

Figure 4. (A) An overview, (B) an SAED pattern and (C) an HRTEM image for the region marked in (A) of a representative ZnO NR after 1.5 Li insertion per each formula unit of ZnO (no extraction). All of the indexed spots for ZnO, and the polycrystalline rings for Zn are also indicated. In the HRTEM image, lattice spacings of 0.28 and 0.205 nm, indicative of ZnO (100) and Zn (101) planes, are denoted. This result as well as an index mapping in (B) verifies the suggested conversion reaction (equation 1 in the text).

2.25 Li per ZnO, the PSD peak becomes weaker and the distribution turns broader into a larger width regime. This pore growth might result from the growth of zinc nanograins during the zinc lithium formation process in the reaction 2. Each porosity data point in Fig. 5 was obtained from more than 20 battery cells and must be therefore highly representative.

Based on the reactions 1 and 2, along with relatively sharp peaks in the PSDs, we propose a pore formation mechanism: a bi-component diffusion process that exhibits a Kirkendall-like effect between the fast-diffusing Zn in the Zn nanograins (after charging via equation 1) and the relatively slowly-diffusing O^{2-} ions in the Li_2O matrix. The unbalanced diffusion between these two components leads to a nanograin-to-pore transition. Hollow nanoparticles driven by a similar Kirkendall effect between fast-diffusing cobalt ions and slowly-diffusing oxide or sulfide ions have been reported.[35] Hence, the zinc nanograins function as templates, directing the pore formation. The similar size (1 ∼ 8 nm) between the nanograins[20] and pore widths as well as the narrow PSDs further supports this hypothesis.

The crystal structures of porous ZnO NRs, like the pore evolution, also undergo gradual changes as the pores progresses. As the Li amount inserted and extracted increases, the NR crystal structure gradually transforms from single-crystalline to poly-crystalline. The crystal structure was studied by SAED patterns (Fig. 6A). Up to the point of 1.8 Li per ZnO inserted and extracted, the spots in the SAED patterns appear as clear dots because the pore evolution is limited to near the surface so that the original crystal structure remains in the cores of NRs. As pores gradually penetrate to the cores of the NRs and porous layers become thicker (Fig. 1), the spots in the SAED patterns become streakier and eventually ring-like, indicating a crystal structure shift toward poly-crystalline. At the point of 2.25 Li per ZnO inserted and extracted, porous ZnO NRs still exhibit a crystal structure close to the original, a so-called crystal mosaic, as indicated by the streaky diffraction pattern in its SAED. From a close investigation of HRTEM images, it is confirmed that the crystal mosaic, a transition state toward poly-crystalline, consists of domains in which lattice orientations are slightly misaligned with neighboring ones. Considering that the entire NRs are covered by pores inside and out at this point, the appearance of the crystal structure close to the original is striking. As NRs become more porous after this point (∼2.25 Li per ZnO), the misaligning becomes more significant, and therefore the crystal structure continuously shifts further away from the original. HRTEM images also show recovered ZnO crystal structures for the entire Li range of $x = 0 \sim 2.95$. In addition, the pore progress can be visualized qualitatively by TEM. Light contrast in the bright field images, indicating void space, appears to progress from the surfaces to the cores of NRs as the Li amount inserted and extracted increases (Fig. 6B), which is consistent with the porosity results. Lattice spacings of ∼2.6 Å are indicative of the (002) ZnO planes (Fig. 6C ∼ 6E), which is the NR growth direction. However, when the amount of Li per ZnO inserted and extracted reaches 2.95, clear domains (Fig. 6E) reflective of a poly-crystalline NR structure were observed. The trend between the porosity and crystal structure is consistent over multiple NRs explored in this SAED study.

A similar pore evolution from the surfaces to the cores of NRs was observed when multiple Li-battery cycles were carried out (Fig. 7). In each cycle, the bottom cutoff potential was fixed at 0.5 V vs. Li/Li^+, which corresponds to 1.5 Li per ZnO insertion/extraction in Fig. 3. We chose this cutoff potential because 1.5 Li per ZnO insertion/extraction is in the proper range that allows for the stepwise pore progression from the surfaces to the cores of ZnO NRs over repeated cycles. With the fixed cutoff potentials, ZnO NRs were cycled up to 10 cycles. As in Fig. 5, BET surface area, BJH pore volume, and PSD data during

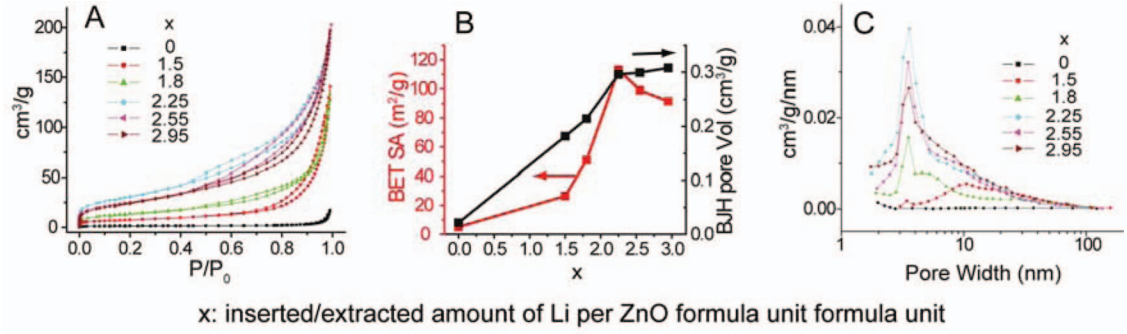

Figure 5. The porosity data including (A) isotherms, (B) BET surface areas and BJH pore volumes, and (C) PSDs indicate the surface-to-core pore evolution. The pore volumes in (B) and the PSDs in (C) are obtained from desorption branches of the BJH method.

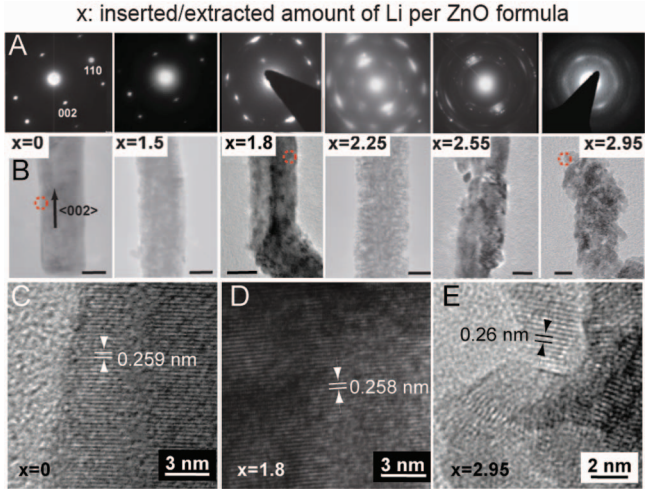

Figure 6. The crystal structure evolution upon various amounts of Li inserted and extracted (=x value). (A) SAED patterns and (B) bright field TEM images of porous ZnO NRs indicate a crystal structure shift from single-crystalline to crystal mosaic to poly-crystalline with the increasing x values. Scale bars in (B) are 30 nm. (C), (D), and (E) are HRTEM images corresponding to the red circled regions in (B). These HRTEM images verify the consistent crystal structure shift toward the poly-crystalline structure as the x value increases.

these cycles indicate that pores are confined to the surfaces and thus are exposed to the space outside NRs (Fig. 7A and 7B). In the subsequent cycles, pores progress toward the cores of NRs. However, even after 10 cycles, the pores do not reach the core as the BET surface area after 10 cycles is still smaller than that of $x = 2.25$ in Fig. 5. These porosity data indicate that pore evolution during the 10 cycles corresponds to the one during x values from 1.5 to some point slightly after 1.8 in Fig. 5. The crystal structures during this period (SAEDs in Fig. 7C) also provide a consistent picture: crystal structure evolution during the 10 cycles corresponds to the one during x values from 1.5 to some point slightly after 1.8 in Fig. 6. The SAED dots after 10 cycles appear more elongated than those of $x = 1.8$, but less elongated than those of $x = 2.25$. Therefore, these multiple cycle data fill the period of $1.5 < x < 2.25$ with more dense porosity points and thus imply that the number of cycle with an appropriate potential control can be a more delicate tool to tune the porosity and crystal structure of the NRs.

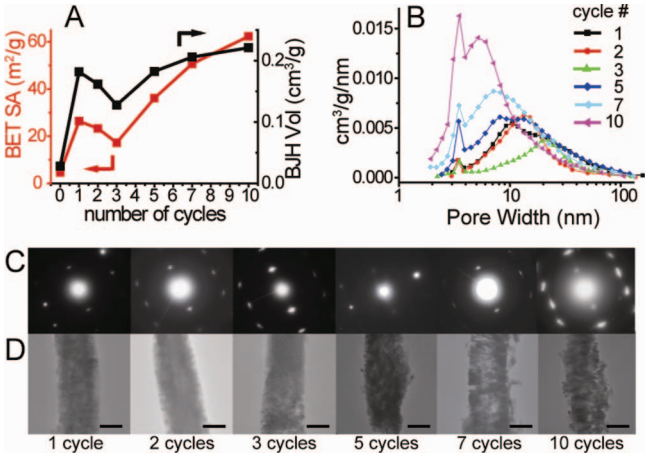

Figure 7. The porosity and crystal structure data when ZnO NRs are cycled multiple times with a fixed cutoff potential at 0.5 V (vs. Li/Li$^+$). The C-rate was 0.1 C. (A) BET surface areas and BJH pore volumes, (B) PSDs, (C) SAEDs, and (D) TEM overviews at 1 ~ 10 cycles. Scale bars in D) are 50 nm.

Conclusions

In summary, we utilize Li-battery cycles to transform nonporous ZnO NRs to porous NRs. Not only have we observed that 1D ZnO nanostructures can become porous through Li-battery cycles such that their surface areas increase by up to 23 times compared to those of as-grown NRs, but we have also found an interesting nanopore evolution depending on the degree of lithiation in the charging process and the number of cycles. In the crystal structure viewpoint, it was observed that the more porous the NRs become, the more difficult it is for the original crystal structure to be recovered. Strikingly, the NRs exhibit the crystal structures close to the original even after a significant portion of the NRs becomes porous. Overall, the pore evolution and the crystal structure shift were simultaneously monitored in a stepwise manner throughout the pore progression from the surfaces to the cores of the NRs. The correlated understanding between these two properties provides a detailed view on the battery processes of the promising ZnO electrodes during cycling. The combined approach between the porosity and the crystal structure has never been reported for any of metal oxide electrodes. Also, the observed fine control over the porosity and the crystal structure is expected to be readily applicable to other 1D metal oxide nanostructures.

Acknowledgments

We acknowledge the financial support by the National Research Foundation of Korea (NRF) grant funded by the Korea government (MEST) ((NRF-2010-C1AAA001-0029031, NRF-2012M1A2A2026587, and NRF-2012-R1A2A1A01011970) and the World Class University Program (R-31-2008-000-10055-0).

References

1. J. B. Goodenough and Y. Kim, *Chem. Mater.*, **22**, 587 (2010).
2. 2008 Annual Progress Report for the Energy Storage Research and Development Vehicle Technologies Program, in.
3. C. K. Chan, H. L. Peng, G. Liu, K. McIlwrath, X. F. Zhang, R. A. Huggins, and Y. Cui, *Nature Nanotechnol.*, **3**, 31 (2008).
4. Y. S. Hu, R. Demir-Cakan, M. M. Titirici, J. O. Muller, R. Schlogl, M. Antonietti, and J. Maier, *Angew. Chem. Int. Ed.*, **47**, 1645 (2008).
5. M. H. Park, M. G. Kim, J. Joo, K. Kim, J. Kim, S. Ahn, Y. Cui, and J. Cho, *Nano Lett.*, **9**, 3844 (2009).
6. A. Magasinski, P. Dixon, B. Hertzberg, A. Kvit, J. Ayala, and G. Yushin, High-performance lithium-ion anodes using a hierarchical bottom-up approach, in *Nat. Mater.*, **9**. 353 (2010).
7. H. Kim, M. Seo, M. H. Park, and J. Cho, *Angew. Chem. Int. Ed.*, **49**, 2146 (2010).
8. Y. Yu, L. Gu, C. B. Zhu, S. Tsukimoto, P. A. van Aken, and J. Maier, *Adv. Mater.*, **22**, 2247 (2010).
9. B. Hertzberg, A. Alexeev, and G. Yushin, *J. Am. Chem. Soc*, **132**, 8548 (2010).
10. M. T. McDowell, S. W. Lee, I. Ryu, H. Wu, W. D. Nix, J. W. Choi, and Y. Cui, *Nano Lett.*, **11**, 4018 (2011).
11. H. Wu, G. Chan, J. W. Choi, I. Ryu, Y. Yao, M. T. McDowell, S. W. Lee, A. Jackson, Y. Yang, L. B. Hu, and Y. Cui, *Nat. Nanotechnol.*, **7**, 310 (2012).
12. T. H. Hwang, Y. M. Lee, B. S. Kong, J. S. Seo, and J. W. Choi, *Nano Letters*, **12**, 802 (2012).
13. H. M. Jeong, S. Y. Lee, W. H. Shin, J. H. Kwon, A. Shakoor, T. H. Hwang, S. Y. Kim, B. S. Kong, J. S. Seo, Y. M. Lee, J. K. Kang, and J. W. Choi, *Rsc Advances*, **2**, 4311 (2012).
14. C. K. Chan, X. F. Zhang, and Y. Cui, *Nano Lett.*, **8**, 307 (2008).
15. J. Graetz, C. C. Ahn, R. Yazami, and B. Fultz, *J. Electrochem. Soc.*, **151**, A698 (2004).
16. M. H. Seo, M. Park, K. T. Lee, K. Kim, J. Kim, and J. Cho, *Energy Environ. Sci.*, **4**, 425 (2011).
17. K. T. Lee, Y. S. Jung, and S. M. Oh, *J. Am. Chem. Soc.*, **125**, 5652 (2003).
18. G. Derrien, J. Hassoun, S. Panero, and B. Scrosati, *Adv. Mater.*, **19**, 2336 (2007).
19. W. M. Zhang, J. S. Hu, Y. G. Guo, S. F. Zheng, L. S. Zhong, W. G. Song, and L. J. Wan, *Adv. Mater.*, **20**, 1160 (2008).
20. P. Poizot, S. Laruelle, S. Grugeon, L. Dupont, and J. M. Tarascon, *Nature*, **407**, 496 (2000).
21. Z. S. Wu, W. C. Ren, L. Wen, L. B. Gao, J. P. Zhao, Z. P. Chen, G. M. Zhou, F. Li, and H. M. Cheng, *Acs Nano*, **4**, 3187 (2010).
22. H. Kim, D. H. Seo, S. W. Kim, J. Kim, and K. Kang, *Carbon*, **49**, 326 (2011).
23. F. Belliard and J. T. S. Irvine, *J. Power Sources*, **97-8**, 219 (2001).
24. J. P. Liu, Y. Y. Li, R. M. Ding, J. Jiang, Y. Y. Hu, X. X. Ji, Q. B. Chi, Z. H. Zhu, and X. T. Huang, *J. Phys. Chem. C*, **113**, 5336 (2009).
25. Y. H. Tong, J. Cheng, J. Q. Deng, and G. G. Siu, *J. Electrochem. Soc.*, **156**, K82 (2009).
26. H. B. Wang, Q. M. Pan, Y. X. Cheng, J. W. Zhao, and G. P. Yin, *Electrochim. Acta*, **54**, 2851 (2009).

27. L. Taberna, S. Mitra, P. Poizot, P. Simon, and J. M. Tarascon, *Nature Mater.*, **5**, 567 (2006).
28. X. H. Liu, L. Q. Zhang, L. Zhong, Y. Liu, H. Zheng, J. W. Wang, J. H. Cho, S. A. Dayeh, S. T. Picraux, J. P. Sullivan, S. X. Mao, Z. Z. Ye, and J. Y. Huang, *Nano Lett.*, **11**, 2251 (2011).
29. J. Y. Huang, L. Zhong, C. M. Wang, J. P. Sullivan, W. Xu, L. Q. Zhang, S. X. Mao, N. S. Hudak, X. H. Liu, A. Subramanian, H. Y. Fan, L. A. Qi, A. Kushima, and J. Li, *Science*, **330**, 1515 (2010).
30. L. E. Greene, M. Law, J. Goldberger, F. Kim, J. C. Johnson, Y. F. Zhang, R. J. Saykally, and P. D. Yang, *Angew. Chem. Int. Ed.*, **42**, 3031 (2003).
31. Z. R. R. Tian, J. A. Voigt, J. Liu, B. McKenzie, M. J. McDermott, M. A. Rodriguez, H. Konishi, and H. F. Xu, *Nature Mater.*, **2**, 821 (2003).
32. L. Vayssieres, *Adv. Mater.*, **15**, 464 (2003).
33. J. J. Wu and S. C. Liu, *Adv. Mater.*, **14**, 215 (2002).
34. Y. S. Hu, Y. G. Guo, W. Sigle, S. Hore, P. Balaya, and J. Maier, *Nature Mater.*, **5**, 713 (2006).
35. Y. D. Yin, R. M. Rioux, C. K. Erdonmez, S. Hughes, G. A. Somorjai, and A. P. Alivisatos, *Science*, **304**, 711 (2004).
36. C. Q. Zhang, J. P. Tu, Y. F. Yuan, X. H. Huang, X. T. Chen, and F. Mao, *J. Electrochem. Soc.*, **154**, A65 (2007).